High Mannose Content of Mesenchymal Glioblastoma Correlates with Hydroxyl Proton Transfer-Weighted (HPTw) MRI as Non-Invasive Biomarker for Tumor Aggressiveness

Behnaz Ghaemi[1,2], Hernando Lopez-Bertoni[3-5], Shreyas Kuddannaya[1,2], Sophie Sall[6], John Laterra[3-5], Guanshu Liu[1,5], Jeff W.M. Bulte[1-3,5-7,*]

[1]Russell H. Morgan Department of Radiology and Radiological Science, Division of MR Research, the Johns Hopkins University School of Medicine, Baltimore, MD;
[2]Cellular Imaging Section and Vascular Biology Program, Institute for Cell Engineering; the Johns Hopkins University School of Medicine, Baltimore, MD;
[3]Department of Oncology; the Johns Hopkins University School of Medicine, Baltimore, MD;
[4]Department of Neurology, the Johns Hopkins University School of Medicine, Baltimore, MD;
[5]Hugo W Moser Research Institute at Kennedy Krieger; Baltimore, MD;
[6]Department of Biomedical Engineering, the Johns Hopkins University School of Medicine, Baltimore, MD.
[7]Department of Chemical & Biomolecular Engineering, the Johns Hopkins Whiting school of Engineering, Baltimore, MD.

*Corresponding author
Johns Hopkins University
733 N. Broadway
MRB 659
Baltimore, MD 21205
USA
Email: jwmbulte@mri.jhu.edu

Short title: CEST MRI of highly mannosylated aggressive GBM.

One sentence summary: The high mannose content of mesenchymal GBM was used as CEST MRI surrogate biomarker for determining tumor aggressiveness.

ABSTRACT

Glioblastoma (GBM) contains mesenchymal cancer stem cells that drive tumor aggressiveness and recurrence and exhibit aberrant glycosylation during proneural-to-mesenchymal transition. A comprehensive computational analysis of human GBM transcriptomic datasets revealed an upregulation of 13 genes involved in glycan mannosylation compared to normal brain and histopathological staining of a tissue array representing 35 GBM cases revealed elevated mannose levels that correlated with increased expression of the mesenchymal marker CD44. Hydroxyl proton transfer-weighted magnetic resonance imaging (HPTw MRI) detected elevated mannose levels in aggressive human mesenchymal GBM *in vitro* and *in vivo*, but not in GBM with a less aggressive non-mesenchymal phenotype. To establish causation over correlation, inhibiting expression of the mannose-binding lectins LMAN1/2 that regulate intracellular processing of mannosylated proteins decreased the glioma cell HPTw MRI signal. Our findings indicate that HPTw MRI correlates with high mannose and possibly other saccharide levels in mesenchymal GBM cells, serving as a surrogate imaging biomarker for predicting tumor aggressiveness and recurrence.

INTRODUCTION

Glioblastoma (GBM) is a very aggressive primary brain tumor with poor prognosis and high incidence of recurrence (*1, 2*). Gene expression profiling studies in GBM have revealed distinct molecular subtypes (e.g. classical, proneural, and mesenchymal) associated with unique genomic abnormalities and clinical outcomes (*3*). The mesenchymal[3] and mesenchymal-like (*4*) subtypes, as defined by gene signatures, associate with the most aggressive disease, worse prognosis, and resistance to current therapies and recurrence (*5*). Identifying key features of this mesenchymal transition can allow for the development of novel biomarkers to enable early detection of aggressive cell subset and improve patient outcome. Protein glycosylation plays a critical role in multiple cellular processes including cell signaling, cell-extracellular matrix interactions, cell migration, immune modulation, and the maintenance of tissue structure and homeostasis(*6*). Among these, mannose-containing glycoproteins stand out due to their involvement in cellular recognition, trafficking, and immune response regulation (*7*). Aberrant glycosylation, including alterations in mannose residues, occurs during the epithelial-to-mesenchymal transition (EMT) and can enhance cell motility, invasiveness, and survival of tumor cells (*8*).

Currently, precision imaging in oncology has limitations, as dictated by the heterogeneity and spatiotemporal composition of tumor cells and their microenvironment (*9*). In this regard, advancing molecular imaging may allow us to leverage aberrant glycan biology for diagnostic purposes. Chemical exchange saturation transfer magnetic resonance imaging (CEST MRI) is an emerging molecular imaging technique that can detect metabolites and molecules that contain exchangeable amide, amine, and hydroxyl protons (*10, 11*). The hydroxyl (OH) protons present in sugar residues have been exploited as an endogenous CEST MRI biomarker for mucin underglycosylation in adenocarcinoma (*12*) and as exogenous glucose (*13-16*) and dextran (*17, 18*) CEST MRI contrast agents for imaging tumor perfusion and blood-brain barrier leakage. We have recently shown that human mesenchymal stem cells (hMSCs) can be detected by mannose-weighted (MANw) CEST MRI by virtue of the high content of their cell membrane hydroxyl groups that are present in high mannose N-linked glycans (*19*). These findings prompted us to investigate if MANw CEST MRI, hereafter referred to as hydroxyl proton transfer-weighted (HPTw) MRI, can be used to differentiate aggressive GBM with a mesenchymal phenotype from less aggressive non-mesenchymal GBM, with the ultimate goal to develop the HPTw MRI signal

as a surrogate imaging biomarker for tumor aggressiveness, recurrence and subtype classification in patients.

RESULTS

Mesenchymal GBM cells express high levels of mannose and genes regulating mannosylation.

Since mesenchymal transitions play important roles in GBM pathogenesis (*3-5, 20*), we aimed to identify molecular events related to these transitions that occur concurrently with changes in mannosylation. We queried expression of known genes involved in the generation and processing of mannosylated glycans in 3 distinct clinical GBM transcriptomic data sets. This analysis identified 13 relevant genes (LMAN1, LMAN2, LMAN2L, SLC35D2, TMEM5 DPY19L1, DPM3, DPM2, DPM1, DPY19L4, PIGB, FKTN, POMT2) to be consistently upregulated in GBM compared to normal brain **(Fig. 1A)**. Further analysis showed that expression of 4 of these 13 genes (LMAN1, LMAN2, LMAN2L and SLC35D2) is elevated in mesenchymal GBM cells compared to the proneural subtype **(Fig. 1B)**. We also identified positive correlations between LMAN1, LMAN2, SLC35D2 and the mesenchymal marker CD44, but not the proneural marker Prom1 (CD133) in transcriptomic datasets derived from clinical specimens **(Fig. 1C)** and GBM stem cells **(Fig. 1D).** Consistent with these transcriptomic associations, fluorescence-activated cell sorting (FACS) followed by quantitative reverse transcription polymerase chain reaction (qRT-PCR) determined that LMAN1 and LMAN2 are enriched in $CD44^+$ GBM cells compared to their $CD44^-$ counterparts (**Fig. 1E**).

To compare glycan mannosylation and CD44 expression between GBM and normal brain in patient samples, a tissue array consisting of 35 glioblastoma and 5 normal brain specimens was analyzed. Fluorescence imaging revealed an association between mannose and expression of mesenchymal markers CD44 in GBM samples (**Fig. 2A,B**), whereas normal brain tissue exhibited little to no expression of these markers. Analysis of CD44 expression and mannose levels demonstrated a positive correlation ($r=0.65$, $p=0.0003$)(**Fig. 2C**), indicating a connection between elevated mannose levels and mesenchymal phenotypic transitions in GBM.

In vitro HPTw MRI of proneural and mesenchymal GBM correlates to mannose and CD44 co-expression.

Mesenchymal transitions and changes in mannose levels are critical determinants of the tumor and stem cell phenotype in multiple cancers, including GBM (*8, 21, 22*). Our findings so far support the hypothesis that $CD44^+$ mesenchymal GBM cells express high levels of mannose compared to their proneural counterparts and that these molecular differences can be leveraged for "label-free" (i.e., without the use of chemical tags) HPTw MRI detection **(Fig. 3A)**. To test this hypothesis, we used two well-characterized patient-derived human isocitrate dehydrogenase (IDH)-wt GBM neurosphere cell lines that represent the mesenchymal (M1123) and proneural subtypes (GBM1a) (*23, 24*). As expected, GBM1a expresses high levels of the proneural markers CD133, Sox2, and Ascl1 while M1123 expresses high levels of the mesenchymal markers CD44, vimentin (Vim) and Snai1 **(Fig. 3B,C)**. Consistent with these distinct molecular features of proneural and mesenchymal GBM cells, M1123 cells also expressed higher amounts of mannose when cultured as neurospheres in defined serum-free stem cell medium, but not when cultured under differentiating conditions in serum-containing medium **(Fig. 3D, S1A).** Accordingly, the higher levels of mannose correspond to a significantly ($p<0.05$) higher HPT signal at 1.2 ppm, i.e., the CEST signature of OH protons abundantly present in mannose (**Fig. 3E**). Importantly, we observed a significant decrease in mannosylation (**Fig. S2A**) and HPT signal (**Fig. 3F and S1B-D**) in M1123 neurospheres upon serum-induced cell differentiation, conditions that reduce the stem cell phenotype of GBM cells (*25, 26*).

Endogenous mannose-binding lectins LMAN1 and LMAN2 impact mannose levels in mesenchymal GBM cells.

Our computational analyses of GBM clinical specimens identified LMAN1 and LMAN2 as potential regulators of mannose homeostasis in mesenchymal GBM cells. Therefore, we examined the effects of LMAN1 and/or LMAN2 expression inhibition on mannose levels in M1123 neurosphere cells (**Fig. 4A**). qRT-PCR analysis demonstrated that the LMAN1- and LMAN2-specific siRNA oligos block their intended gene targets **(Fig. 4B)** concurrent with a significant reduction in mannose staining **(Fig. 4C,D).** We did not observe an additive effect when we knocked-down LMAN1 and LMAN2 simultaneously, likely reflecting the known overlapping functions of these lectins in the intracellular processing of mannose glycans **(Fig. 4D)**. The decrease in mannose content after specific LMAN1 and LMAN2 knock-down correlated with a decrease in HPTw MRI signal *in vitro* **(Fig. 4E, Fig. S3).**

***In vivo* HPTw MRI of proneural and mesenchymal GBM correlates with mannose levels and CD44 expression.**

We assessed the feasibility of HPTw MRI in differentiating brain tumors derived from proneural vs. mesenchymal GBM neurospheres *in vivo*. Eight-week-old NOD SCID gamma mice received tumor cells in the left (GBM1a) and right (M1123) striatum. MRI was then performed on post-implantation days 1, 8, and 16. M1123-derived tumor xenografts exhibited a significantly higher growth rate concurrent with a prominent HPTw MRI signal that was absent in the GBM1a-derived tumors and normal brain. The HPT signal in M1123 tumors remained consistently elevated (>1.8-fold) compared to GBM1a tumors and normal brain for all three time points, with a characteristic mannose peak around 1.2 ppm **(Fig. 5A,B, Fig. S3)**. We also analyzed tumors using APTw MRI, a technique approved by the FDA in 2018 for its ability to identify active high-grade brain cancer by detecting endogenous proteins and peptides (*27*). This is achieved by measuring the CEST signal at 3.5 ppm (amide protons) that is distinct from the 1.2 ppm signal from hydroxyl protons. Contrasting the HPTw MRI results, APTw MRI did not generate a consistent pattern in distinguishing GBM1a and M1123 tumors throughout the study (**Fig. S4**). APTw MRI signals from M1123 and GBM1a were indistinguishable on day 1. The M1123 APTw MRI signal was significantly higher than the GBM1a signal on day 8 and significantly lower than that from GBM1a signal on day 16 (**Fig. S4A,B**). Immunofluorescent post-mortem staining for mannose and CD44 colocalized with areas of HPTw MRI contrast, demonstrating that the cells with high mannose content represent mesenchymal GBM cells within the orthotopic M1123 tumor xenografts **(Fig. 5C)**. Gadolinium (Gd)-enhanced perfusion MRI, performed eight days post-tumor implantation, revealed no significant differences in perfusion characteristics between GBM1a and M1123 tumors, suggesting similar vascularization and blood-brain barrier permeability (**Fig. S5**).

DISCUSSION

GBM remains one of the most aggressive and treatment-resistant brain tumors, with 14-18 month median survival despite aggressive treatment (*2, 28*). Substantial efforts have been dedicated to characterizing the molecular landscape of GBM cells to understand mechanisms driving therapy resistance (*4, 29*). Gene expression profiling studies in GBM have highlighted

mesenchymal transitions as a key contributor to poor patient outcomes (*3, 30*). Additionally, mesenchymal-like cancer cells exhibit enhanced motility, self-renewal capacity, and resistance to apoptosis and immune evasion (*3, 30*). Single-cell transcriptomic studies have further reinforced the link between mesenchymal transition and therapy resistance (*5, 31*). High-resolution single-cell transcriptomic analyses of GBM tumors before and after standard-of-care therapy demonstrated critical changes in the tumor microenvironment and cell state transitions associated with stemness-driving events and acquisition of mesenchymal signatures (*31*).

Changes in glycosylation profiles are an important feature of mesenchymal transitions (*8*) and offer a potential biomarker for classifying tumor subtypes and monitoring transitions to more aggressive treatment resistant tumors. Among various glycosylation patterns, high mannose-linked glycosylation is a distinct attribute of aggressiveness and may play a fundamental role in therapy resistance (*32*). High-mannose glycosylation has been proposed as a biomarker for aggressive GBM subtypes and enhanced glycosylation is linked to hematopoietic stem cells (*33*) and metabolic reprogramming of mesenchymal GBM stem cells (*34*). Interestingly, a recent study found that GSCs exhibit elevated levels of α-1,2-mannosidase (MAN1C1), an enzyme involved in the processing of N-glycans, and this elevated expression is associated with poor outcomes in glioma patients (*35*). Changes in N-glycosylation driven by MGAT5, an enzyme that adds branching mannose residues to N-glycans, correlates with more invasive phenotype in GSCs (*36*). Consistent with these observations, we show that mesenchymal GBM cells express higher levels of genes involved in mannose regulation **(Fig. 1)** and, for the first time, that mesenchymal GBM neurospheres display significantly higher mannose levels and higher HPTw MRI signal than their proneural counterparts **(Figs. 3,4)**. Importantly, these correlations were maintained in patient-derived glioma cells, GBM tissues and human tumor xenografts **(Figs. 1,2,4),** underscoring the potential value of non-invasive imaging approaches to detect these molecular alterations in clinical settings.

While conventional T2-weighted and Gd-based contrast-enhanced MRI enable visualizing brain tumors, they lack specificity in differentiating tumor subtypes and assessing microenvironmental changes (**Fig. S5**)(*37*). Advanced techniques such as diffusion-weighted imaging and perfusion imaging augment structural imaging with functional information by measuring water diffusion and vascularity (*38*), respectively, while magnetic resonance spectroscopy further aids in tumor characterization by detecting metabolic markers such as

choline and lactate (*39*). However, these modalities insufficiently capture molecular features linked to specific tumor subtypes and their different aggressiveness. APTw MRI detects mobile proteins and peptides and has the ability to differentiate between high and low-grade glioma as well as to distinguish radiation necrosis from recurring tumors (*40, 41*). We now show that HPTw MRI is able to distinguish mesenchymal from proneural experimental GBM xenografts, which can be combined with APTw MRI for imaging different and potentially complementary aspects of GBM pathology, i.e., APTw MRI detecting proteins/peptides and HPTw MRI saccharides.

As for clinical translatability, dynamic glucose-enhanced (DGE) MRI has been successfully performed in many GBM patients around the world, both at 3T and 7T. For all available DGE methods, i.e., conventional CEST (*14, 42, 43*), direct water saturation (*44*), and T1ρ (spin lock-based) (*45-48*) approaches, high field approaches perform better and different field strengths require separate optimization. In the Z-spectrum, both the detection sensitivity and specificity of the 1.2 ppm resonance go down with field strength, due to a faster exchange regime and more mixing with the direct saturation resonance (*49*).

Like most cancers, GBM undergoes metabolic reprogramming to support tumor cell survival, proliferation, and invasion (*50*). Aberrant glycosylation is a notable consequence of this metabolic rewiring, however, our understanding of the role of glycosylation in GBM pathology remains incomplete (*51*). We show here that HPTw MRI can distinguish between proneural and mesenchymal cells and we rigorously show that this is based on their differential mannose content (**Figs. 3,4**). Blocking expression of endogenous mannose-binding lectins, LMAN1 and LMAN2, significantly reduces HPTw MRI signal and mannose-specific lectin staining *in vitro* and *in vivo* **(Fig. 5)**, demonstrating that mannose is directly responsible as a contributor for the HPTw MRI signal in mesenchymal GBM cells. However, as the HPTw MRI signal detects hydroxyl protons from all saccharides, mannose may not be solely responsible for the increased signal, and in certain contexts other overexpressed glycans might also contribute. Future studies on direct quantitative validation of mannose content by ^{1}H NMR spectroscopy, liquid chromatography-mass spectrometry (LC-MS), or preferably matrix-assisted laser desorption/ionization (MALDI) MS imaging may provide further insight into their relative contributions. Indeed, Angerstein et al. performed spatial N-glycan MALDI-MSI on human GBM and reported elevated high-mannose species in GBM tissue specimens (*52*). These

findings independently support our observation that mannose is elevated in GBM and provide histopathology-linked spatial evidence in patient tissue, in agreement with our human tissue array staining for mannose (Fig. 2A).

Integrating HPTw MRI with the currently available MRI portfolio, including APTw MRI, could enable a more comprehensive evaluation of GBM. We envision this approach will improve detection of aggressive mesenchymal tumors and their recurrence, refine treatment stratification, enhance the monitoring of therapeutic responses, and aid in optimizing surgical planning. This new imaging approach could be easily interfaced with current clinical imaging protocols to positively impact patient outcomes.

MATERIALS AND METHODS

Study design

The aim of this study was to assess whether the presence of high mannose content in GBM correlates to the expression of the mesenchymal marker CD44, and if such high mannosylation can be detected with HPTw MRI in GBM with an aggressive mesenchymal phenotype. Known genes involved in the generation and processing of mannosylated glycans were analyzed in 3 distinct clinical GBM transcriptomic data sets (GlioVis database) (*53*). LMAN1/LMAN2 were identified as one of the major overexpressed proteins and further analyzed by qRT-PCR in $CD44^+$ and $CD44^-$ GBM cells. Thirty-five GBM specimens from a tissue array were stained for mannose and CD44 co-expression with 5 normal brain specimens serving as control. $CD44^-$ proneural (GBM1a) and $CD44^+$ mesenchymal (M1123) mouse GBM cells were analyzed for mannose content and *in vitro* HPTw MRI contrast at 11.7T. siRNA-mediated specific knockdown of LMAN1/LMAN2 expression in M1123 cells was confirmed by qRT PCR analysis and its resulting effect on mannosylation assessed by immunofluorescent staining and *in vitro* HPTw MRI. GBM1a and M1123 were implanted bilaterally in immunodeficient mice and imaged in vivo for up to 16 days. Mice were randomly grouped, and sample sizes were based on prior experiments and literature. Post-mortem staining for mannose and CD44 was correlated to the regions-of-interest containing MRI contrast. Information about the number of biological replicates and times that experiments were replicated is given in the respective figure legends and in the methods section. No data were excluded from the study. All

animal experiments were approved by the Animal Care and Use Committee at Johns Hopkins University School of Medicine.

Patient databases

Clinical and transcriptomic data from control and glioma patient samples was retrieved from the GlioVis database (http:// gliovis.bioinfo.cnio.es/)(*53*).

Glioblastoma tissue array

A tissue microarray, containing 35 cases of glioblastoma and 5 cases of normal cerebral tissue (duplicate cores per case) was obtained from Tissuearray.com (GL805-L51). CD44 expression and mannose levels were calculated by measuring mean fluorescence intensity (MFI) from fluorescence images, with values normalized on a 0–100% scale for comparison across samples.

Cell culture

Human 20913 (GBM1a) cells were initially established by Vescovi and colleagues(*23*) and characterized by our group (*54*). M1123 cells were generously provided by Dr. Nakano (Ohio State University)(*34*). Neurospheres were maintained in serum-free medium supplemented with epidermal growth factor (EGF) and fibroblast growth factor (FGF) and cultured in ultra-low-attachment 6-well plates (Millipore-Sigma) at 37°C under 5% CO_2/95% air. Serum-induced differentiation was performed by introducing serum into the culture medium and transitioning the cells to adherent conditions in T-25 flasks.

Immunofluorescent staining for CD44 and mannose

GBM1a and M1123 neurospheres were transferred in 1-well cell culture chamber slides. Cells were first incubated in cold PBS containing 20 µg/ml GNL-FITC (FL-1241, Vector Laboratories) at 4 °C for 50 minutes for the presence of mannose, then washed three times with PBS. They were fixed with 4% paraformaldehyde for 20 min at room temperature (RT) and permeabilized using 0.1% Triton X-100 in PBS for 10 min. After blocking non-specific binding sites with 5% normal goat serum (NGS), cells were incubated with primary Alexa Fluor® 647 anti-CD44 antibody (1:250, Abcam, EPR18668) according to the manufacturer's protocol (3 h at

RT in the dark). Excess antibody was removed by washing 3x with 10 mM phosphate buffered saline, pH=7.4 (PBS). Nuclei were stained with 4′,6-diamidino-2-phenylindole (DAPI) for 5 minutes. To stain the tissue array slides, they were deparaffinized by sequential washes in xylene (2×5 minutes), followed by rehydration through a graded ethanol series (100%, 95%, 70%, and 50%, 5 minutes each) and a final rinse in distilled water. For antigen retrieval, slides were incubated in sodium citrate buffer (10 mM, pH=6.0) at 95–100°C for 20 minutes, then allowed to cool to RT before washing three times with PBS. For immunostaining, slides were blocked in 5% bovine serum albumin (BSA) in PBS for 1 hour at room temperature to minimize non-specific binding. Tissue arrays were then incubated with Alexa Fluor® 647 anti-CD44 antibody (1:250) and 20 µg/ml of GNL (Galanthus nivalis lectin)-FITC for 1 hour at RT in the dark. Unbound antibody/lectin was removed by washing three times with PBS. Nuclei were counterstained with DAPI for 5 minutes, followed by a final PBS wash. All fluorescence imaging was performed using a Zeiss Axiovert 200 M inverted epifluorescence microscope, using consistent exposure settings for FITC and Alexa Fluor® 647. For quantification of CD44 expression and the mannosylation score using fluorescent images, background fluorescence was subtracted uniformly across all images. Using Zen2 software (Zeiss core imaging software) ROIs were drawn around each tissue core, excluding any folded or damaged areas. Mean fluorescence intensity values for GNL-FITC (mannose) and Alexa Fluor® 647 (CD44) were measured and normalized onto a 1–100 scale by assigning the lowest measured intensity a value of 1 and the highest a value of 100. These normalized data were then used to determine the correlation between CD44 expression and mannosylation score.

Knockdown of LMAN1 and LMAN2

For M1123 cells, the mannose-binding lectins LMAN1 and LMAN2 were knocked down using liposomal transfection with LMAN 1/2 siRNA (Millipore-Sigma, Cat# SASI_Hs01_00189318 and SASI_Hs01_00209153), and LMAN1/2 expression was quantified with qRT-PCR and normalized to GAPDH. siRNA transfections were performed using RNAiMax (Thermo Fisher Scientific) according to the manufacturer's recommendations. Briefly, GBM neurosphere single-cell suspensions ($2.5x10^5$ cells) were seeded onto ultra-low-attachment 24-well plates (Millipore-Sigma) in 800 µL of neurosphere medium. Lipofectamine RNAiMax reagent (12 µL) was added to 100 µL of Opti-MEM medium. In a separate tube,

siRNA oligos were diluted in 100 µL of Opti-MEM to achieve a final concentration of 240 nM. Tubes were combined, mixed and incubated at RT for 15 minutes to allow lipid-siRNA complex formation. The mixture was then added dropwise to GBM neurospheres single-cell suspensions. Cells were collected 5 days after transfections for gene expression analysis.

qRT-PCR

Total RNA was extracted from the cells using a RNeasy mini kit (Qi-agen, Germantown, MD). cDNA was made by reverse-transcribing 1 µg of total RNA using MuLV Reverse Transcriptase and Oligo (dT) primers (Applied Biosystems,Waltham, MA). qRT-PCR was performed with the Bio-Rad CFX detection System (BioRad, Hercules, CA), and the expression of target genes was measured using the Power SYBR green PCR kit (Applied Biosystems). The samples were amplified in triplicate, and relative gene expression was analyzed using Bio-Rad CFX manager software v3.1 and normalized to 18S RNA. The primer sequences used in this study were obtained from PrimerBank (https://pga.mgh.harvard.edu/primerbank/, last accessed on 12.20.24) and are listed in **Table S1**.

***In vitro* HPTw MRI**

For *in vitro* HPTw MRI studies, 1×10^6 GBM1a and M1123 neurospheres with an average size of 500 µm were collected, rinsed three times with PBS, and loaded into 5 mm NMR tubes (Wilmad®, USA). Imaging was then conducted on an 11.7 T Bruker Biospin vertical bore scanner equipped with a 20 mm birdcage transmit/receive coil. A modified RARE (rapid acquisition with refocused echoes) sequence was employed, with the following parameters: repetition time (TR)/echo time (TE)=6,000/5 ms, RARE factor=32, number of averages (NA)=2, slice thickness=1 mm, field of view (FOV)=16×16 mm, matrix size = 64×64, in-plane resolution=0.25×0.25 mm, B_1=2.4 µT, and saturation time (T_{sat})=4 s. A relatively high saturation pulse (B1=2.4 µT) was chosen because the exchange rate of mannose is fast, approximately 2,700 Hz at 37 °C and pH=7.4 (**Fig. S6**). Saturation frequencies ranged from −5 to +5 ppm in 0.2 ppm intervals, with 0 ppm referencing the water resonance. The total acquisition time was 20 min and 48 s. LMAN1-, LMAN2-, and dual LMAN1/2–knockdown neurospheres were subsequently imaged under identical conditions and compared with WT M1123. All experiments were performed as three independent replicates.

Animal Model

All animal procedures were approved by the Johns Hopkins University Animal Care and Use Committee. Immunodeficient NSG mice (NOD.Cg-Prkdc^{scid} Il2rg^{tm1Wjl}/SzJ) were obtained from Jackson Laboratories (Bar Harbor, ME, USA) and maintained as an in-house breeding colony. Male and female mice, aged 8 weeks (22–25 g), were housed under a 12-hour light/dark cycle with unrestricted access to food and water. During all surgery and imaging procedures, mice were anesthetized with isoflurane (2–3% for induction and 1–2% for maintenance in O_2), using a calibrated vaporizer and scavenging system. Breathing rate and body temperature were continuously monitored and controlled throughout the scanning procedure. For stereotaxic injections, a burr hole was drilled at coordinates 0 mm caudal and 2 mm lateral to the bregma on each side. A Hamilton syringe was used to inject 2.5 µL of single cell suspensions from neurospheres. Neurospheres were dissociated into single cells using gentle mechanical trituration and enzymatic treatment with Accutase. Spheres were first pipetted gently using a wide-bore tip, followed by incubation in pre-warmed StemPro™ Accutase™ cell dissociation reagent (Gibco, USA) at 37°C for 20 minutes, with occasional swirling to obtain a single-cell suspension. Cells (1.5×10^5 M1123 or GBM1A in PBS) were injected into the right and left striatum at a depth of 2 mm below the endocranium, administered at a rate of 0.2 µL min^{-1}. To compare the perfusion properties of GBM1a and M1123 tumors, mice received 0.2 mmol/kg of a Gd-based contrast agent (Omniscan, Nycomed, Oslo, Norway) via a pre-inserted intravenous catheter. Dynamic T1-weighted imaging was conducted before injection (baseline) and continuously for 10 minutes post-injection to evaluate perfusion and vascular permeability.

***In vivo* HPTw, APTw, and Gd-enhanced T1w MRI**

MRI was carried out on days 1, 8, and 16 post-transplantation using an 11.7 T Bruker Biospec preclinical scanner (Bruker, Ettlingen, Germany) with a 23-mm volume transmit/receive coil coil. T2-weighted (T2w) MRI parameters were TR/TE=3,000/5.6 ms, RARE factor=16, slice thickness=1 mm, FOV=1.6×1.5 cm, matrix=256×128, and NA=3. HPTw and APTw MRI parameters were TR/TE=5,500/3.7 ms, RARE factor=23, single slice, slice thickness= 1 mm, FOV=1.6×1.6 cm, matrix=64×64, NA=1, B_1=2.4 µT, and T_{sat}=3 s, with saturation frequencies ranging from −5 to +5 ppm in 0.25 ppm increments (water signal set to 0 ppm). The total

acquisition time was 7 minutes. Tumor and brain regions of interest (ROIs) were manually drawn from T2-w images. This experiment was performed in five independent replicates. Gd-enhanced MRI was performed by i.v. injection of ProHance® (0.1 mmol/kg, bolus over about 10 s, injection volume =50 µL, injection rate= 5 µL/s). A single-slice FLASH gradient echo sequence (TR/TE=18/3 ms, and flip angle =15°) was used to acquire DCE images at the same position and spatial resolution as the CEST images. The acquisition started two minutes before injection. The total acquisition time of DCE MRI was 13 min at temporal resolution of 14.6 s.

Post-mortem tissue analysis

Mice were transcardially perfused with 10 mM PBS and 4% paraformaldehyde (PFA). The brain was removed and re-immersed in 4% PFA at 4 °C for 24 h, then transferred to 30% sucrose for another 72 h. After embedding in optimal cutting temperature (OCT) compound, the brain was cryosectioned into 10 µm sections. For GNL and anti-CD44 staining, brain sections were first rehydrated with PBS for 10 min and then incubated with 20 µg/ml FITC-GNL and 1:250 Alexa Fluor® 647 anti-CD44 antibody for 1h at RT. After washing 3x with PBS, sections were coverslipped using mounting medium containing DAPI. Fluorescence microscopy was performed using a Zeiss Axiovert 200 M inverted epifluorescence microscope.

Statistical analysis

For statistical analysis of patient data, pairwise comparisons between group levels with corrections for multiple testing (p values with Bonferroni correction) were used. Pearson's correlation analysis was performed to assess relationships between CD44 expression and mannosylation score, and linear regression models were applied to visualize trends with 95% confidence intervals. Data are presented as mean±standard deviation (SD and were analyzed using a one-way analysis of variance (ANOVA), followed by Dunnett's post hoc test for multiple group comparisons, with significance thresholds set at *$p<0.05$, ** $p<0.01$, and ***$p<0.001$ and ****$p<0.0001$. Comparisons between tumors were performed using a two-tailed Student's t-test. Sample sizes were determined to achieve adequate statistical power (>90%, $p=0.01$) for detecting expected effect sizes, estimated based on our preliminary data and prior experience with similar experiments. The number of independent repetitions for each experiment is given in the corresponding figure captions. All statistical analyses were conducted using

GraphPad Prism 6.0. Investigators remained blinded to group allocations during and after experiments including MRI data processing.

List of Supplementary Materials(*55*)

Figs. S1 to S6

Table S1

REFERENCES AND NOTES

1. Q. T. Ostrom, M. Price, C. Neff, G. Cioffi, K. A. Waite, C. Kruchko, J. S. Barnholtz-Sloan, CBTRUS Statistical Report: Primary Brain and Other Central Nervous System Tumors Diagnosed in the United States in 2015-2019. *Neuro Oncol* **24**, v1-v95 (2022).
2. R. Stupp, W. P. Mason, M. J. van den Bent, M. Weller, B. Fisher, M. J. Taphoorn, K. Belanger, A. A. Brandes, C. Marosi, U. Bogdahn, J. Curschmann, R. C. Janzer, S. K. Ludwin, T. Gorlia, A. Allgeier, D. Lacombe, J. G. Cairncross, E. Eisenhauer, R. O. Mirimanoff, R. European Organisation for, T. Treatment of Cancer Brain, G. Radiotherapy, G. National Cancer Institute of Canada Clinical Trials, Radiotherapy plus concomitant and adjuvant temozolomide for glioblastoma. *N Engl J Med* **352**, 987-996 (2005).
3. R. G. Verhaak, K. A. Hoadley, E. Purdom, V. Wang, Y. Qi, M. D. Wilkerson, C. R. Miller, L. Ding, T. Golub, J. P. Mesirov, G. Alexe, M. Lawrence, M. O'Kelly, P. Tamayo, B. A. Weir, S. Gabriel, W. Winckler, S. Gupta, L. Jakkula, H. S. Feiler, J. G. Hodgson, C. D. James, J. N. Sarkaria, C. Brennan, A. Kahn, P. T. Spellman, R. K. Wilson, T. P. Speed, J. W. Gray, M. Meyerson, G. Getz, C. M. Perou, D. N. Hayes, N. Cancer Genome Atlas Research, Integrated genomic analysis identifies clinically relevant subtypes of glioblastoma characterized by abnormalities in PDGFRA, IDH1, EGFR, and NF1. *Cancer Cell* **17**, 98-110 (2010).
4. C. Neftel, J. Laffy, M. G. Filbin, T. Hara, M. E. Shore, G. J. Rahme, A. R. Richman, D. Silverbush, M. L. Shaw, C. M. Hebert, J. Dewitt, S. Gritsch, E. M. Perez, L. N. Gonzalez Castro, X. Lan, N. Druck, C. Rodman, D. Dionne, A. Kaplan, M. S. Bertalan, J. Small, K. Pelton, S. Becker, D. Bonal, Q. D. Nguyen, R. L. Servis, J. M. Fung, R. Mylvaganam, L. Mayr, J. Gojo, C. Haberler, R. Geyeregger, T. Czech, I. Slavc, B. V. Nahed, W. T. Curry, B. S. Carter, H. Wakimoto, P. K. Brastianos, T. T. Batchelor, A. Stemmer-Rachamimov, M. Martinez-Lage, M. P. Frosch, I. Stamenkovic, N. Riggi, E. Rheinbay, M. Monje, O. Rozenblatt-Rosen, D. P. Cahill, A. P. Patel, T. Hunter, I. M. Verma, K. L. Ligon, D. N. Louis, A. Regev, B. E. Bernstein, I. Tirosh, M. L. Suva, An Integrative Model of Cellular States, Plasticity, and Genetics for Glioblastoma. *Cell* **178**, 835-849 e821 (2019).

5. F. S. Varn, K. C. Johnson, J. Martinek, J. T. Huse, M. P. Nasrallah, P. Wesseling, L. A. D. Cooper, T. M. Malta, T. E. Wade, T. S. Sabedot, D. Brat, P. V. Gould, A. Woehrer, K. Aldape, A. Ismail, S. K. Sivajothi, F. P. Barthel, H. Kim, E. Kocakavuk, N. Ahmed, K. White, I. Datta, H. E. Moon, S. Pollock, C. Goldfarb, G. H. Lee, L. Garofano, K. J. Anderson, D. Nehar-Belaid, J. S. Barnholtz-Sloan, S. Bakas, A. T. Byrne, F. D'Angelo, H. K. Gan, M. Khasraw, S. Migliozzi, D. R. Ormond, S. H. Paek, E. G. Van Meir, A. M. E. Walenkamp, C. Watts, T. Weiss, M. Weller, K. Palucka, L. F. Stead, L. M. Poisson, H. Noushmehr, A. Iavarone, R. G. W. Verhaak, G. Consortium, Glioma progression is shaped by genetic evolution and microenvironment interactions. *Cell* **185**, 2184-2199 e2116 (2022).
6. A. Bellahcene, V. Castronovo, K. U. Ogbureke, L. W. Fisher, N. S. Fedarko, Small integrin-binding ligand N-linked glycoproteins (SIBLINGs): multifunctional proteins in cancer. *Nat Rev Cancer* **8**, 212-226 (2008).
7. H. Jin, X. Liu, H. X. Liu, Biological function, regulatory mechanism, and clinical application of mannose in cancer. *Biochim Biophys Acta Rev Cancer* **1878**, 188970 (2023).
8. M. Pucci, N. Malagolini, F. Dall'Olio, Glycobiology of the Epithelial to Mesenchymal Transition. *Biomedicines* **9**, (2021).
9. H. Hricak, M. E. Mayerhoefer, K. Herrmann, J. S. Lewis, M. G. Pomper, C. P. Hess, K. Riklund, A. M. Scott, R. Weissleder, Advances and challenges in precision imaging. *Lancet Oncol* **26**, e34-e45 (2025).
10. P. C. van Zijl, N. N. Yadav, Chemical exchange saturation transfer (CEST): what is in a name and what isn't? *Magn Reson Med* **65**, 927-948 (2011).
11. K. M. Ward, A. H. Aletras, R. S. Balaban, A new class of contrast agents for MRI based on proton chemical exchange dependent saturation transfer (CEST). *J Magn Reson* **143**, 79-87 (2000).
12. X. Song, R. D. Airan, D. R. Arifin, A. Bar-Shir, D. K. Kadayakkara, G. Liu, A. A. Gilad, P. C. van Zijl, M. T. McMahon, J. W. Bulte, Label-free in vivo molecular imaging of underglycosylated mucin-1 expression in tumour cells. *Nat Commun* **6**, 6719 (2015).
13. L. Knutsson, X. Xu, P. C. M. van Zijl, K. W. Y. Chan, Imaging of sugar-based contrast agents using their hydroxyl proton exchange properties. *NMR Biomed* **36**, e4784 (2023).

14. X. Xu, N. N. Yadav, L. Knutsson, J. Hua, R. Kalyani, E. Hall, J. Laterra, J. Blakeley, R. Strowd, M. Pomper, P. Barker, K. Chan, G. Liu, M. T. McMahon, R. D. Stevens, P. C. van Zijl, Dynamic Glucose-Enhanced (DGE) MRI: Translation to Human Scanning and First Results in Glioma Patients. *Tomography* **1**, 105-114 (2015).
15. K. W. Chan, M. T. McMahon, Y. Kato, G. Liu, J. W. Bulte, Z. M. Bhujwalla, D. Artemov, P. C. van Zijl, Natural D-glucose as a biodegradable MRI contrast agent for detecting cancer. *Magn Reson Med* **68**, 1764-1773 (2012).
16. S. Walker-Samuel, R. Ramasawmy, F. Torrealdea, M. Rega, V. Rajkumar, S. P. Johnson, S. Richardson, M. Goncalves, H. G. Parkes, E. Arstad, D. L. Thomas, R. B. Pedley, M. F. Lythgoe, X. Golay, In vivo imaging of glucose uptake and metabolism in tumors. *Nat Med* **19**, 1067-1072 (2013).
17. Y. Li, Y. Qiao, H. Chen, R. Bai, V. Staedtke, Z. Han, J. Xu, K. W. Y. Chan, N. Yadav, J. W. M. Bulte, S. Zhou, P. C. M. van Zijl, G. Liu, Characterization of tumor vascular permeability using natural dextrans and CEST MRI. *Magn Reson Med* **79**, 1001-1009 (2018).
18. G. Liu, S. R. Banerjee, X. Yang, N. Yadav, A. Lisok, A. Jablonska, J. Xu, Y. Li, M. G. Pomper, P. van Zijl, A dextran-based probe for the targeted magnetic resonance imaging of tumours expressing prostate-specific membrane antigen. *Nat Biomed Eng* **1**, 977-982 (2017).
19. Y. Yuan, C. Wang, S. Kuddannaya, J. Zhang, D. R. Arifin, Z. Han, P. Walczak, G. Liu, J. W. M. Bulte, In vivo tracking of unlabelled mesenchymal stromal cells by mannose-weighted chemical exchange saturation transfer MRI. *Nat Biomed Eng* **6**, 658-666 (2022).
20. A. Dirkse, A. Golebiewska, T. Buder, P. V. Nazarov, A. Muller, S. Poovathingal, N. H. Brons, S. Leite, N. Sauvageot, D. Sarkisjan, Stem cell-associated heterogeneity in Glioblastoma results from intrinsic tumor plasticity shaped by the microenvironment. *Nature communications* **10**, 1787 (2019).
21. Y. Wei, Q. Chen, S. Huang, Y. Liu, Y. Li, Y. Xing, D. Shi, W. Xu, W. Liu, Z. Ji, The interaction between DNMT1 and high-mannose CD133 maintains the slow-cycling state and tumorigenic potential of glioma stem cell. *Advanced Science* **9**, 2202216 (2022).

22. F. Papaccio, F. Paino, T. Regad, G. Papaccio, V. Desiderio, V. Tirino, Concise review: cancer cells, cancer stem cells, and mesenchymal stem cells: influence in cancer development. *Stem cells translational medicine* **6**, 2115-2125 (2017).
23. R. Galli, E. Binda, U. Orfanelli, B. Cipelletti, A. Gritti, S. De Vitis, R. Fiocco, C. Foroni, F. Dimeco, A. Vescovi, Isolation and characterization of tumorigenic, stem-like neural precursors from human glioblastoma. *Cancer Res* **64**, 7011-7021 (2004).
24. A. L. Johnson, H. S. Khela, J. Korleski, S. Sall, Y. Li, W. Zhou, K. Smith-Connor, H. Lopez-Bertoni, J. Laterra, TGFBR2-High mesenchymal glioma stem cells phenocopy regulatory T cells to suppress CD4+ and CD8+ T cell function. *bioRxiv*, 2025.2001.2007.631757 (2025).
25. V. F. Fiore, J. Almagro, E. Fuchs, Shaping epithelial tissues by stem cell mechanics in development and cancer. *Nature Reviews Molecular Cell Biology*, (2025).
26. H. Lopez-Bertoni, B. Lal, A. Li, M. Caplan, H. Guerrero-Cazares, C. G. Eberhart, A. Quinones-Hinojosa, M. Glas, B. Scheffler, J. Laterra, Y. Li, DNMT-dependent suppression of microRNA regulates the induction of GBM tumor-propagating phenotype by Oct4 and Sox2. *Oncogene* **34**, 3994-4004 (2015).
27. J. Zhou, M. Zaiss, L. Knutsson, P. Z. Sun, S. S. Ahn, S. Aime, P. Bachert, J. O. Blakeley, K. Cai, M. A. Chappell, M. Chen, D. F. Gochberg, S. Goerke, H. Y. Heo, S. Jiang, T. Jin, S. G. Kim, J. Laterra, D. Paech, M. D. Pagel, J. E. Park, R. Reddy, A. Sakata, S. Sartoretti-Schefer, A. D. Sherry, S. A. Smith, G. J. Stanisz, P. C. Sundgren, O. Togao, M. Vandsburger, Z. Wen, Y. Wu, Y. Zhang, W. Zhu, Z. Zu, P. C. M. van Zijl, Review and consensus recommendations on clinical APT-weighted imaging approaches at 3T: Application to brain tumors. *Magn Reson Med* **88**, 546-574 (2022).
28. A. L. Ling, I. H. Solomon, A. M. Landivar, H. Nakashima, J. K. Woods, A. Santos, N. Masud, G. Fell, X. Mo, A. S. Yilmaz, Clinical trial links oncolytic immunoactivation to survival in glioblastoma. *Nature* **623**, 157-166 (2023).
29. L. Wang, J. Jung, H. Babikir, K. Shamardani, S. Jain, X. Feng, N. Gupta, S. Rosi, S. Chang, D. Raleigh, A single-cell atlas of glioblastoma evolution under therapy reveals cell-intrinsic and cell-extrinsic therapeutic targets. *Nature cancer* **3**, 1534-1552 (2022).
30. H. S. Phillips, S. Kharbanda, R. Chen, W. F. Forrest, R. H. Soriano, T. D. Wu, A. Misra, J. M. Nigro, H. Colman, L. Soroceanu, P. M. Williams, Z. Modrusan, B. G. Feuerstein,

K. Aldape, Molecular subclasses of high-grade glioma predict prognosis, delineate a pattern of disease progression, and resemble stages in neurogenesis. *Cancer Cell* **9**, 157-173 (2006).

31. J. Wang, E. Cazzato, E. Ladewig, V. Frattini, D. I. Rosenbloom, S. Zairis, F. Abate, Z. Liu, O. Elliott, Y.-J. Shin, Clonal evolution of glioblastoma under therapy. *Nature genetics* **48**, 768-776 (2016).
32. K. Scupakova, O. T. Adelaja, B. Balluff, V. Ayyappan, C. M. Tressler, N. M. Jenkinson, B. S. Claes, A. P. Bowman, A. M. Cimino-Mathews, M. J. White, P. Argani, R. M. Heeren, K. Glunde, Clinical importance of high-mannose, fucosylated, and complex N-glycans in breast cancer metastasis. *JCI Insight* **6**, (2021).
33. H. Hemmoranta, T. Satomaa, M. Blomqvist, A. Heiskanen, O. Aitio, J. Saarinen, J. Natunen, J. Partanen, J. Laine, T. Jaatinen, N-glycan structures and associated gene expression reflect the characteristic N-glycosylation pattern of human hematopoietic stem and progenitor cells. *Experimental hematology* **35**, 1279-1292 (2007).
34. P. Mao, K. Joshi, J. Li, S. H. Kim, P. Li, L. Santana-Santos, S. Luthra, U. R. Chandran, P. V. Benos, L. Smith, M. Wang, B. Hu, S. Y. Cheng, R. W. Sobol, I. Nakano, Mesenchymal glioma stem cells are maintained by activated glycolytic metabolism involving aldehyde dehydrogenase 1A3. *Proc Natl Acad Sci U S A* **110**, 8644-8649 (2013).
35. D. C. Batara, H. J. Kim, L. T. Phan, M. Kim, Y. O. Son, S. Lee, S. I. Park, Y. S. Choi, S. Beck, S. H. Kim, Elevated alpha-1,2-mannosidase MAN1C1 in glioma stem cells and its implications for immunological changes and prognosis in glioma patients. *Sci Rep* **14**, 22159 (2024).
36. E. Marhuenda, C. Fabre, C. Zhang, M. Martin-Fernandez, T. Iskratsch, A. Saleh, L. Bauchet, J. Cambedouzou, J. P. Hugnot, H. Duffau, J. W. Dennis, D. Cornu, N. Bakalara, Glioma stem cells invasive phenotype at optimal stiffness is driven by MGAT5 dependent mechanosensing. *J Exp Clin Cancer Res* **40**, 139 (2021).
37. S. Lescher, A. Jurcoane, A. Veit, O. Bähr, R. Deichmann, E. Hattingen, Quantitative T1 and T2 mapping in recurrent glioblastomas under bevacizumab: earlier detection of tumor progression compared to conventional MRI. *Neuroradiology* **57**, 11-20 (2015).

38. P. Svolos, E. Kousi, E. Kapsalaki, K. Theodorou, I. Fezoulidis, C. Kappas, I. Tsougos, The role of diffusion and perfusion weighted imaging in the differential diagnosis of cerebral tumors: a review and future perspectives. *Cancer Imaging* **14**, 1-20 (2014).
39. C. Choi, S. K. Ganji, R. J. DeBerardinis, K. J. Hatanpaa, D. Rakheja, Z. Kovacs, X.-L. Yang, T. Mashimo, J. M. Raisanen, I. Marin-Valencia, 2-hydroxyglutarate detection by magnetic resonance spectroscopy in IDH-mutated patients with gliomas. *Nature medicine* **18**, 624-629 (2012).
40. C. H. Suh, J. E. Park, S. C. Jung, C. G. Choi, S. J. Kim, H. S. Kim, Amide proton transfer-weighted MRI in distinguishing high- and low-grade gliomas: a systematic review and meta-analysis. *Neuroradiology* **61**, 525-534 (2019).
41. J. Zhou, E. Tryggestad, Z. Wen, B. Lal, T. Zhou, R. Grossman, S. Wang, K. Yan, D.-X. Fu, E. Ford, Differentiation between glioma and radiation necrosis using molecular magnetic resonance imaging of endogenous proteins and peptides. *Nature medicine* **17**, 130-134 (2011).
42. J. Mo, X. Xu, A. Ma, M. Lu, X. Wang, Q. Rui, J. Zhu, H. Wen, G. Lin, L. Knutsson, P. van Zijl, Z. Wen, Dynamic glucose-enhanced MRI of gliomas: A preliminary clinical application. *NMR Biomed* **38**, e5265 (2025).
43. X. Xu, K. W. Chan, L. Knutsson, D. Artemov, J. Xu, G. Liu, Y. Kato, B. Lal, J. Laterra, M. T. McMahon, P. C. van Zijl, Dynamic glucose enhanced (DGE) MRI for combined imaging of blood-brain barrier break down and increased blood volume in brain cancer. *Magn Reson Med* **74**, 1556-1563 (2015).
44. L. Knutsson, N. N. Yadav, S. Mohammed Ali, D. O. Kamson, E. Demetriou, A. Seidemo, L. Blair, D. D. Lin, J. Laterra, P. C. M. van Zijl, Dynamic glucose enhanced imaging using direct water saturation. *Magn Reson Med* **94**, 15-27 (2025).
45. D. Paech, P. Schuenke, C. Koehler, J. Windschuh, S. Mundiyanapurath, S. Bickelhaupt, D. Bonekamp, P. Bäumer, P. Bachert, M. E. Ladd, M. Bendszus, W. Wick, A. Unterberg, H. P. Schlemmer, M. Zaiss, A. Radbruch, T1ρ-weighted Dynamic Glucose-enhanced MR Imaging in the Human Brain. *Radiology* **285**, 914-922 (2017).
46. B. Bender, K. Herz, A. Deshmane, V. Richter, G. Tabatabai, J. Schittenhelm, M. Skardelly, K. Scheffler, U. Ernemann, M. Kim, X. Golay, M. Zaiss, T. Lindig, GLINT:

GlucoCEST in neoplastic tumors at 3 T-clinical results of GlucoCEST in gliomas. *MAGMA* **35**, 77-85 (2022).

47. T. Jin, B. Iordanova, T. K. Hitchens, M. Modo, P. Wang, H. Mehrens, S. G. Kim, Chemical exchange-sensitive spin-lock (CESL) MRI of glucose and analogs in brain tumors. *Magn Reson Med* **80**, 488-495 (2018).
48. K. Herz, T. Lindig, A. Deshmane, J. Schittenhelm, M. Skardelly, B. Bender, U. Ernemann, K. Scheffler, M. Zaiss, T1rho-based dynamic glucose-enhanced (DGErho) MRI at 3 T: method development and early clinical experience in the human brain. *Magn Reson Med* **82**, 1832-1847 (2019).
49. P. C. M. van Zijl, W. W. Lam, J. Xu, L. Knutsson, G. J. Stanisz, Magnetization Transfer Contrast and Chemical Exchange Saturation Transfer MRI. Features and analysis of the field-dependent saturation spectrum. *Neuroimage* **168**, 222-241 (2018).
50. S. Chugh, V. S. Gnanapragassam, M. Jain, S. Rachagani, M. P. Ponnusamy, S. K. Batra, Pathobiological implications of mucin glycans in cancer: Sweet poison and novel targets. *Biochimica et Biophysica Acta (BBA)-Reviews on Cancer* **1856**, 211-225 (2015).
51. L. Rosa-Fernandes, S. M. Oba-Shinjo, J. Macedo-da-Silva, S. K. N. Marie, G. Palmisano, Aberrant Protein Glycosylation in Brain Cancers, with Emphasis on Glioblastoma. *Adv Exp Med Biol* **1382**, 39-70 (2022).
52. A. O. Angerstein, L. E. A. Young, T. Thanasupawat, J. Vriend, G. Grimsley, X. Lun, D. L. Senger, N. Sinha, J. Beiko, M. Pitz, S. Hombach-Klonisch, R. R. Drake, T. Klonisch, Distinct spatial N-glycan profiles reveal glioblastoma-specific signatures. *J Pathol* **265**, 486-501 (2025).
53. R. L. Bowman, Q. Wang, A. Carro, R. G. Verhaak, M. Squatrito, GlioVis data portal for visualization and analysis of brain tumor expression datasets. *Neuro Oncol* **19**, 139-141 (2017).
54. Y. Li, A. Li, M. Glas, B. Lal, M. Ying, Y. Sang, S. Xia, D. Trageser, H. Guerrero-Cázares, C. G. Eberhart, A. Quiñones-Hinojosa, B. Scheffler, J. Laterra, c-Met signaling induces a reprogramming network and supports the glioblastoma stem-like phenotype. *Proc Natl Acad Sci U S A* **108**, 9951-9956 (2011).

55. M. Zaiss, G. Angelovski, E. Demetriou, M. T. McMahon, X. Golay, K. Scheffler, QUESP and QUEST revisited - fast and accurate quantitative CEST experiments. *Magn Reson Med* **79**, 1708-1721 (2018).

Acknowledgments: We thank Bachchu Lal for performing cryosectioning, Dr. Calixto-Hope G. Lucas Jr. for his advice on the glioblastoma tissue array and neuropathology, and Drs. Kristine Glunde, Peter C.M. van Zijl, Asif Itoo, and Janani Gurumurthy for discussing methods for detecting elevated saccharide levels, its specificity, and clinical translatability. **Funding:** This study was funded by NIH grants R01 EB030376 (JWMB), R01 NS120949 (HLB), R01 NS073611 (JL), R01 NS096754 (JL), R01 CA261974 (GL), the Sidney Kimmel Comprehensive Cancer Center Translational Research Central Services Shared Resource (P30 CA006973), the Clinical Translation Core at the Kennedy Krieger Institute (5P50 HD103538), and the Maryland Stem Cell Research Fund grants 2023-MSCRFD-6135 (JWMB) and 2025-R2-MSCRFD-00026 (JWMB). As this manuscript is the result of funding in whole or in part by the National Institutes of Health (NIH), it is subject to the NIH Public Access Policy. Through acceptance of this federal funding, NIH has been given a right to make this manuscript publicly available in PubMed Central upon the Official Date of Publication, as defined by NIH. **Author contributions:** B.G. and J.W.M.B. conceived the ideas for initiating this study. H.L-B. performed computational analysis of transcriptomic datasets. B.G., H.L-B., G.L., and J.W.M.B. designed the methods and experimental design. B.G., H.L-B., S.K. S.S, C-H.G.L.Jr. and G.L. performed in vitro cell and in vivo animal experiments and data analysis. B.G. and H.L-B. wrote the initial manuscript draft. J.W.M.B. and H.L-B. acquired the funding for this project. All authors read, edited and revised the manuscript. **Competing interests:** B.G. and J.W.M.B. have a pending patent, #PCT/US25/18274, filed March 4 2025: J.W.M. Bulte, B. Ghaemi: Methods and related aspects for grading glioblastoma aggressiveness. All others have nothing to disclose. **Data and code availability:** The data generated in this study have been deposited in the Johns Hopkins Research Data Repository under accession code https://doi.org/10.7281/T15AV9PY. Source data are provided with this paper. Standard CEST MRI data processing Matlab codes are available at https://godzilla.kennedykrieger.org/CEST/. All correspondence should be sent to J.W.M.B.

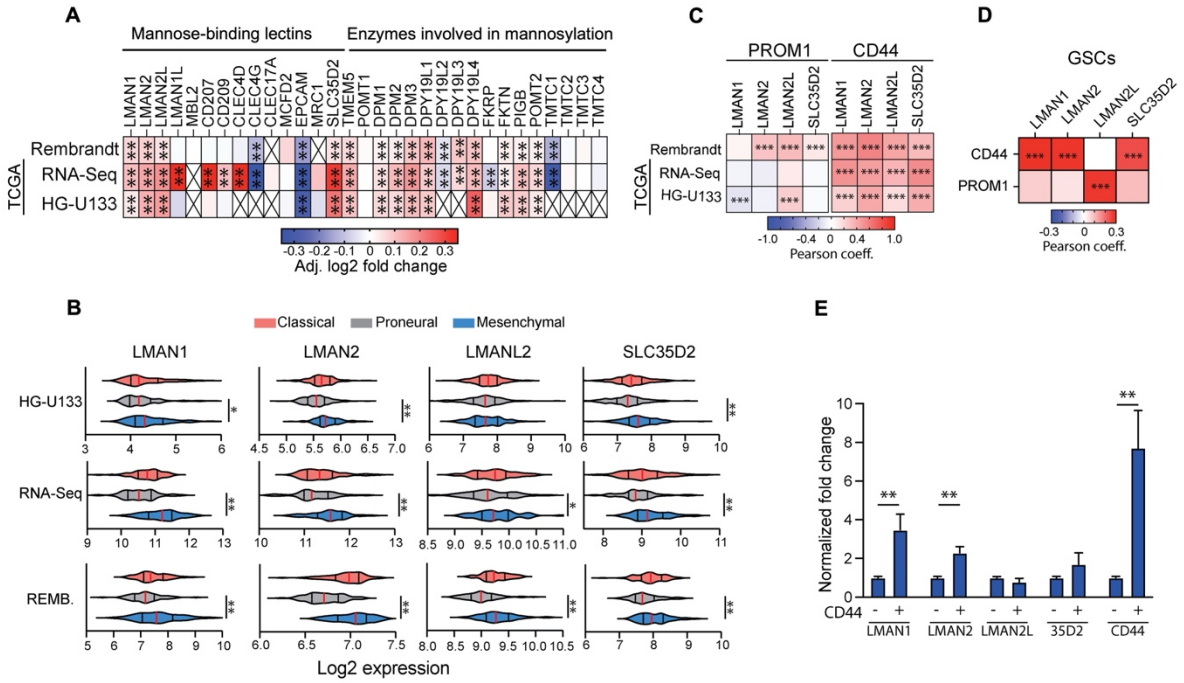

Figure 1: LMAN1 and LMAN2 are enriched in mesenchymal GBM cells. (A) Expression of genes coding for regulators of mannose metabolism was compared between IDH-wt GBM and normal brain tissue. Upregulated genes are shown in red. **(B)** Violin plots showing expression of LMAN1, LMAN2, LMAN2L, and SLC35D2 in different GBM molecular subtypes. Correlation matrix showing Pearson's coefficients between the mesenchymal marker CD44 or prominin and LMAN1, LMAN2, LMAN2L, and SLC35D2 in GBM clinical specimens **(C)** and primary GBM neurospheres **(D)**. **(E)** qRT-PCR to measure expression of LMAN1, LMAN2, LMAN2L, and SLC35D2 in GBM neurospheres sorted into CD44 positive and negative populations. Statistical significance was calculated using unpaired, non-parametric, student's t-test with Mann-Whitney post hoc test in panels **A, B;** statistical significance was calculated using Student's t-test in panel **E.** Expression data was retrieved from the clinical databases using the GlioVis portal (http://gliovis.bioinfo.cnio.es)(*53*). *p<0.05, **p<0.01; ***p<0.001; X=not determined.

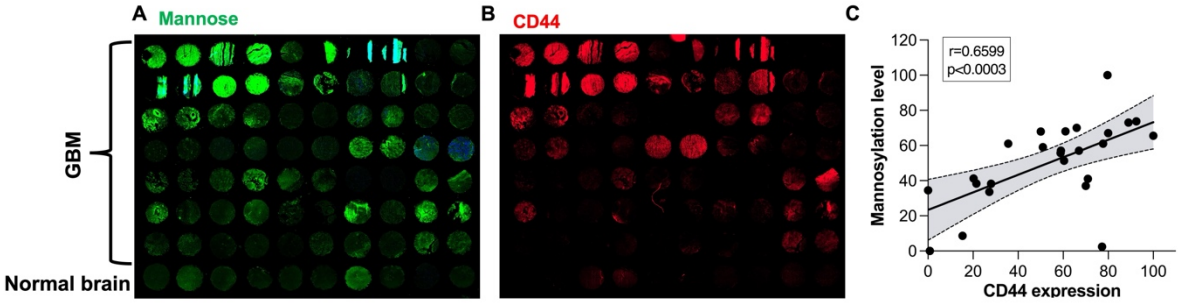

<u>Figure 2:</u> Tissue array of GBM reveals the co-presence of mannose and CD44, which correlate to tumor aggressiveness. Clinical tissue array containing 35 different GBM (patients aged 8-80 years) and 5 normal human cerebral tissue samples (for a total of 80 in duplicate) were stained for (**A**) mannose and (**B**) the mesenchymal marker CD44. (**C**) Scatter plots with linear regression lines show the relationship between CD44 expression and mannose levels in GBM tissue samples. Shaded gray areas represent 95% confidence intervals.

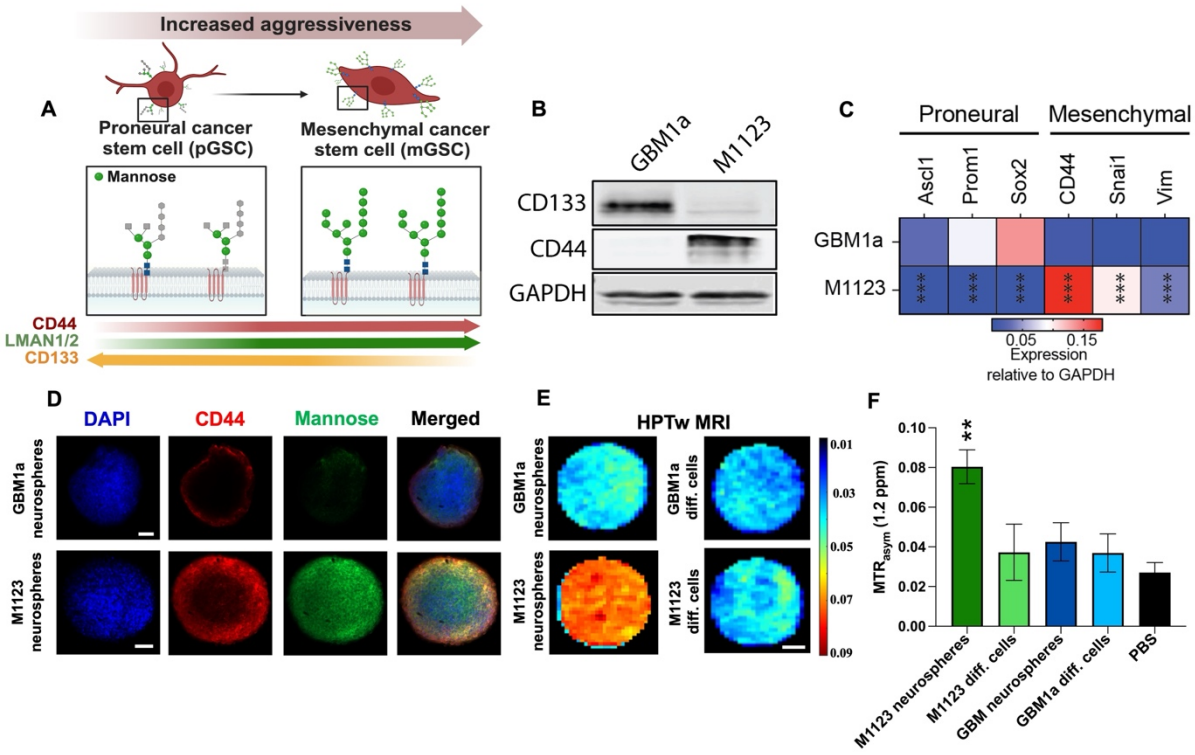

<u>Figure 3:</u> ***In vitro*** **HPTw MRI signal corresponds to mannose and CD44 co-expression in mesenchymal GBM which is absent in proneural GBM. (A)** Schematic illustration of the proneural-to-mesenchymal transition in GBM, resulting in elevated mannose N-linked glycan levels in $CD44^+$ mesenchymal cells which is absent in $CD133^+$ proneural cells. (**B**) Western blot showing expression of CD133 (proneural) and CD144 (mesenchymal) markers in GBM1a and M1123 cells. (**C**) qRT-PCR analysis of canonical proneural and mesenchymal markers in GBM1a and M1123 cells. **(D)** Mannose and CD44 staining in single representative GBM1a and M1123 neurospheres. Scale bar=200 µm. (**E**) *In vitro* HPTw MRI and (**F**) signal quantification of GBM1a and M1123 neurospheres suspended in a 5 mm NMR tube. Scale bar in (**E**)=1 mm. Statistical significance was determined using Student's t-test, where **p<0.01.

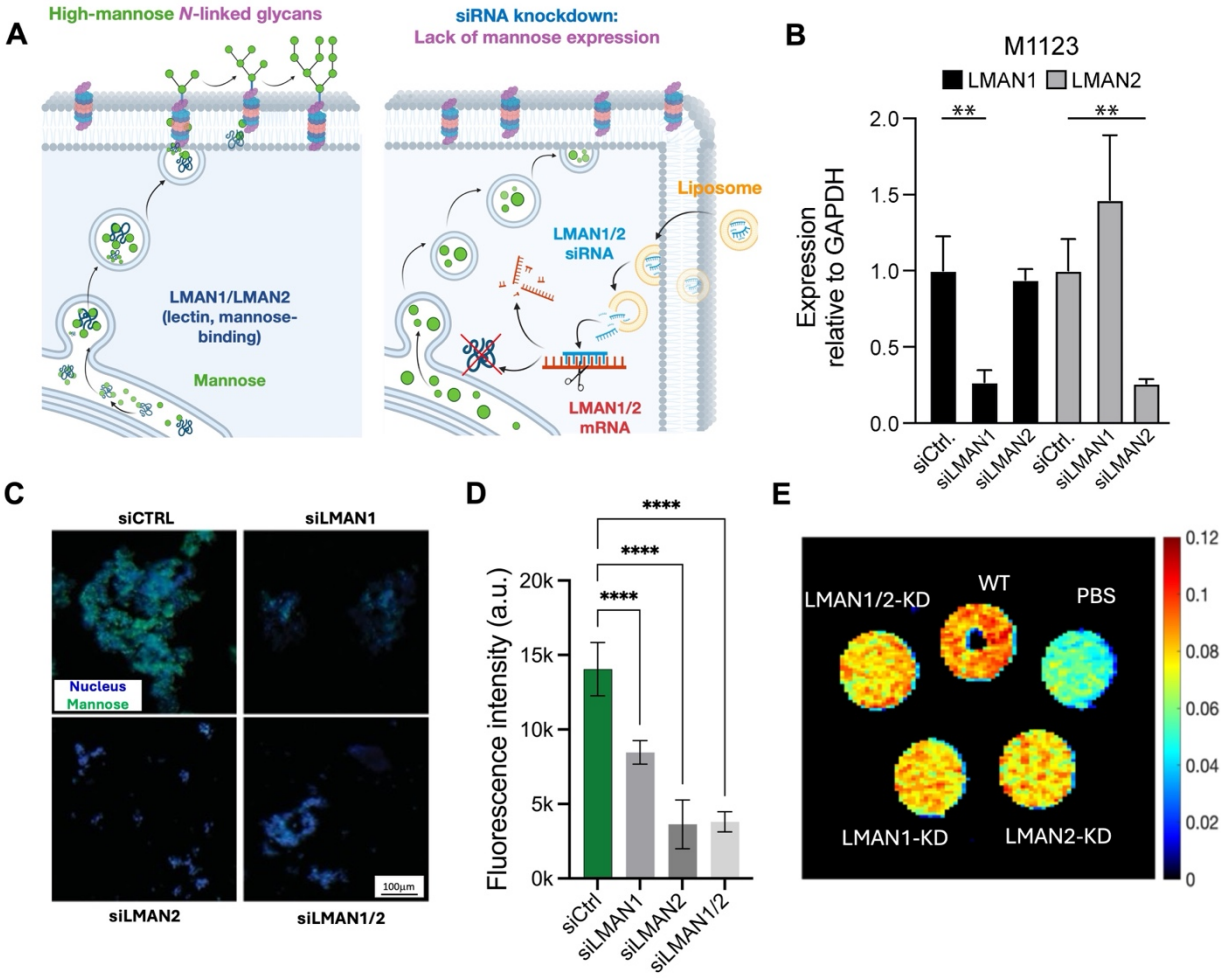

<u>Figure 4:</u> Knockdown of LMAN1 and LMAN2 in M1123 cells decreases mannosylation and HPTw MRI contrast. (**A**) Schematic outline of siRNA-mediated silencing of LMAN1/2. (**B**) qRT PCR analysis shows specific knockdown of LMAN1 and LMAN2 compared to control siRNA and LMAN cross-control siRNA. (**C**) Mannose staining and (**D**) quantification. (**E**) *In vitro* HPTw MRI signal at 1.2 ppm for wild type (WT) cells and LMAN1/LMAN2 knockdown cells. Statistical significance was calculated using one-way ANOVA with Tukey's post hoc test in panels B and D. Statistical significance was determined using one-way ANOVA, where **p<0.01 and ****p<0.0001.

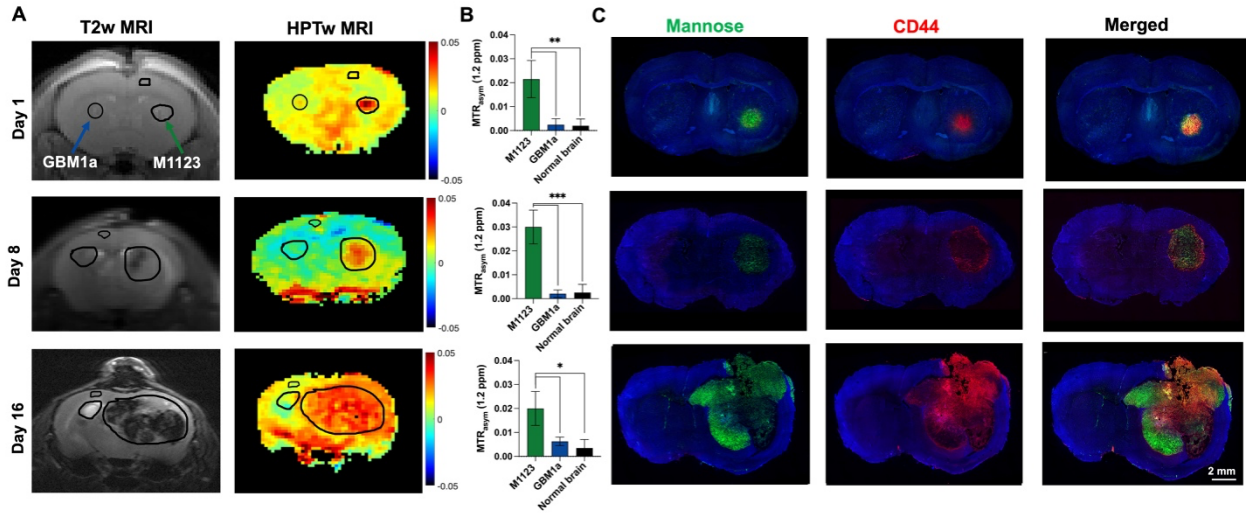

<u>Figure 5:</u> ***In vivo*** **HPTw MRI signal corresponds to mannose and CD44 co-expression in mesenchymal GBM which is absent in proneural GBM**. **(A)** Serial *in vivo* T2-weighted and HPTw MRI of a bilateral orthotopic GBM1a and M1123 mouse xenograft model at different time points post tumor implantation. (**B**) Quantified HPTw MRI signal at 1.2 ppm for the regions of interest drawn in A as an example for n=5 animals. (**C**) FITC-GNL and anti-CD44 staining in tissue sections representative for the brain slices shown in A. Statistical significance was determined using one-way ANOVA, where $p<0.05$; $^{**}p<0.01$ and $^{***}p<0.001$.